Reduced order models for uncertainty quantification of gas plumes from leakages during LNG bunkering

Vinh-Tan Nguyen [a,*], Venugopalan S.G. Raghavan [a], Raymond Y.L. Quek [a], Lim Boon How [b], Deguang Yan [c]

[a] *Institute of High Performance Computing, 1 Fusionopolis Way, #16-16 Connexis, 138632, Singapore*
[b] *Sembcorp Marine, 80 Tuas South Boulevard, 637051, Singapore*
[c] *ABS Singapore Innovation & Research Center 438B Alexandra Road Alexandra Technopark, 119968, Singapore*

A R T I C L E I N F O

Keywords:
Liquefied natural gas
Jet leak
Risk analysis
Computational fluid dynamics
Uncertainty quantification

A B S T R A C T

The impacts of uncertainty in wind conditions on the spread of hazardous plume resulting from a jet leak during a Liquefied Natural Gas (LNG) bunkering operation were investigated. Computational Fluid Dynamics (CFD) using the Reynolds-Averaged Navier Stokes (RANS) solver with multi-species transport and a transient leak model for keyhole leak was used for the simulation of a simplified bunkering station. Following detailed validation & verification, the sensitivity of the safety zone extents to the wind conditions was demonstrated. CFD results reinforced the strong dependence of the maximum spread distance on wind conditions and enclosure geometry. To quantify the impact of input uncertainty from wind conditions on the plume spread, a reduced-order model (ROM) was developed using the proper orthogonal decomposition (POD) of CFD results on sampled conditions. ROM-POD enables a fast evaluation of the plume under changing wind conditions and acts as an efficient forward model for uncertainty quantification using Polynomial Chaos Expansion (PCE) technique. The spatial distribution of plume residence time under the same input uncertainty was also obtained from the proposed approach showing its potential in risk assessment and design of bunkering facilities.

1. Introduction

Liquefied natural gas (LNG) is a mixture of predominantly methane (80%–99%) together with other alkanes (ethane, propane and butane) and a small portion of nitrogen (up to 1%). Condensed into the liquid state at a low temperature of about −162 °C, LNG is very efficiently stored with 600 times more volume compared to its gaseous phase. It also has very low emissions of sulphur & nitrogen oxides and other particulate matters compared to traditional fossil fuels. Consequently, LNG has become a leading alternative source of marine fuel in the face of increasingly stringent pollution requirements in the shipping industry (Thomson et al., 2015). This increased demand has led to growing interest in the development of bunkering infrastructure from many stakeholders in industries and academia.

Given the complexity of bunkering operations and the intrinsic cryogenic nature of LNG, a key aspect in developing LNG bunkering is the risk assessment of accidents associated with LNG bunkering facilities and operations. Among the many risks associated with LNG bunkering facilities and operations, LNG spills and leakage are the most hazardous events. Cracks and defects in the pipes are likely to cause a release of gas or liquid as under-expansion jets due to pressurized conditions in the pipe. The strength and complexity of the jet depend on the ratio of the ambient pressure to the pressure at the end of the opening on the pipe.

Additionally, given the conditions under which LNG is stored, a spill rapidly evaporates (on land or water) and forms an initially cold, heavy vapour plume. The plume is blown downwind, warms up, and may eventually become positively buoyant, and may lift off to become a dilute elevated vapour cloud. The vapour cloud can ignite and burn as a flash fire or pool fire. Plume explosions are possible in congested liquefaction or regasification plants but less likely in other situations (Woodward and Pitblado, 2010).

A large number of parameters affect the dispersion of gases. These include atmospheric stability, wind speed, local terrain effects, leak hole geometries and release locations, momentum and buoyancy of the material released. Assessment and definition of the safety zone during LNG bunkering has thus become critical in mitigating the risks. Regulatory frameworks and guidelines for the design and operation of LNG bunkering facilities are still under active development across the world (McInerney et al., 2014; Xu et al., 2015), including this extensive

* Correspondence to: 1 Fusionopolis Way, #16-16 Connexis, 138632, Singapore.
E-mail address: nguyenvt@ihpc.a-star.edu.sg (V.-T. Nguyen).

https://doi.org/10.1016/j.jlp.2022.104724
Received 22 March 2021; Received in revised form 28 December 2021; Accepted 2 January 2022
Available online 19 January 2022

guideline on LNG bunkering control (Society for Gas as a Marine Fuel, 2018).

There exists a wide range of risk analysis approaches in the literature to identify hazards, evaluate the probability of accidents as well as the assessment of consequences associated with LNG facilities. A comprehensive review of risk assessment methods was presented in Animah and Shafiee (2020) with a detailed classification framework for different methodologies currently employed for LNG risk analysis. Among those approaches, Computational Fluid Dynamics (CFD) is gaining popularity in the community as a more accurate model for capturing most of the fundamental physics in LNG accidents. CFD was also recommended by an earlier study (Koopman and Ermak, 2007) as the most complete model to describe the rich physics in gas dispersion process in LNG spills. As the highest fidelity approach for modelling gas dispersion, it solves the 3-dimensional Navier–Stokes flow equations without limitations in the domain and geometrical complexity. This allows real geometries to be investigated with complex terrain characteristics, obstacles and transitions.

CFD models have been widely applied to simulate the gas dispersion (Sun et al., 2013; Giannissi et al., 2013; Park et al., 2018; Eberwein et al., 2020) and validated with experimental data. All these models solve continuity, momentum, energy, and species transport to calculate the concentration of gas. Particular attention has to be paid to turbulence modelling, as the turbulent eddies significantly influence the gas dispersion process. The effects of turbulence can be modelled using Reynolds-Averaged Navier–Stokes (RANS) approach, Large Eddy Simulations (LES) or fully simulated through Direct Numerical Simulations (DNS). Unfortunately, DNS is very computationally demanding, making it currently applicable only to very simple cases. An intermediate solution is to solve only large eddies using LES. While LES is less demanding than DNS, it places severe resource constraints for complex geometries. Consequently, RANS represents a good compromise between accuracy and computational effort. One of the most popular closure models for the RANS approach is the $k-\epsilon$ two-equation model since it assures good stability and reasonable results for gas dispersion simulations (Luketa-Hanlin et al., 2007; Sun et al., 2013).

As highlighted earlier, the leaks typically result in under-expansion jets due to pressurized conditions in the pipe. Generally, the structure of such an under-expanded jet is characterized by three main zones: the near-field, transition, and far-field regions (Franquet et al., 2015). Flow structures are highly complex in the near-field region, typically composed of normal shocks and their reflection causing Mach disc and triple points. Modelling this near field region requires resolving complex flow features of compressible flows. In the far-field region, the jet is fully expanded and achieves self-similarity. Conditions from this region are used in our current simulations to model the release.

It is impractical to fully resolve under-expanded jets in a release due to its requirement of various length scales. While the structures of the under-expanded jets are well understood in the literature, resolving it in simulations requires very fine resolution and high computational resources. Given the scale of most typical jet leaks in practical applications, resolving the near field under-expanded jet is prohibitively expensive. Alternatively, the whole under-expanded jet region can be represented as a pseudo-source from which the jet is released to the ambient. Taking into account the gas expansion from an orifice exit to far-field, the pseudo-source normally provides fully developed flow conditions at an equivalent plane as a boundary condition to CFD codes. There are several pseudo-source models developed in the literature for this purpose and one can refer to Franquet et al. (2015) for a detailed review of the available models.

There are many factors affecting how the natural gas spreads and forms a flammable cloud resulting from a leak (Society for Gas as a Marine Fuel, 2018), many detailed previously. In particular, for environmental conditions such as wind speed and direction, there is a large uncertainty in the input due to inherently varying conditions of the wind. It is thus desirable to quantify impacts of this uncertainty on the assessment of risk associated with LNG leakage. To quantify the uncertainty propagation through computational models, there are various techniques depending on the types of uncertainties as well as the representation of output uncertainty (Helton et al., 2004). For aleatory uncertainties, both sampling approach (e.g. Monte-Carlo, Latin hypercube sampling (LHS)) and stochastic methods (e.g. polynomial chaos expansion (PCE)) are often applied for characterizing propagation of uncertainties through the numerical models (Xiu, 2009).

Quantifying the impact of uncertainty of input parameters in a leak event requires evaluation of a considerable number of scenarios. Fast and efficient forward models are preferable for this purpose. Given a probability distribution of the input, sampling-based approach will evaluate the output quantities of interest at various sample points one-by-one to build a discrete representation of the output responses. For traditional random sampling, aka Monte-Carlo approach, a large number of samples are required to accurately determine the output distribution. In LHS, each input variable is divided into N-bins of equal probability and a sample point is uniformly determined from a unique bin for each variable, thus avoiding clustering of samples. LHS requires fewer sample points compared to random sampling for the same accuracy. Alternatively, to alleviate the problem of large sample size, a response function can be built from a limited number of sample points using PCE. This approximation is considered as a surrogate model to the more expensive computational model and allows evaluation of a much larger number of output functions for a more accurate distribution. For a detailed review on the stochastic methods, one can refer to the earlier work (Xiu, 2009) and the references cited therein.

In this work, we present a study on the assessment of gas cloud spread due to a leak in an LNG bunkering station under uncertain wind conditions. Simulations of the gas dispersion process were performed using the RANS model coupled with a transient leak sub-model for capturing LNG release in the near field of under-expanded jets. For comprehensive risk assessment of the leak and for uncertainty quantification, a fast reduced-order model (ROM) was developed using the proper orthogonal decomposition (POD) interpolation technique. In this method, offline snapshots of CFD simulations for a range of wind conditions were sampled to provide the POD modes for subsequent interpolation at a new condition. With the ROM-POD, the uncertainty quantification of wind speed and direction of gas cloud spread was carried out using PCE technique. The results obtained showed that wind speed and direction caused large changes in the extent of the cloud with a mean spread distance of about 60 metres from the centre of the leak and a variance of about 15 metres for a sample windrose data in Singapore. The ROM also showed its potential in providing useful input in the spatial distribution of hazardous gas clouds for the future design of bunkering facilities.

The rest of the paper is organized as follows. In Section 2, details of the CFD methodology are presented with a summary of the RANS solver and the transient leak model used for performing high fidelity simulations. In Section 3, analysis of the impact of wind conditions on gas cloud spread from a bunkering station is shown, demonstrating a strong influence of environmental parameters on gas dispersion. Section 4 addresses the uncertainty quantification of wind speed and direction on the maximum spread of gas cloud from a LNG leak. And finally, Section 5 presents concluding remarks.

2. Methodologies

Gas leaks into the atmosphere present a complex multi-physics problem coupling physics from multiple disciplines like fluid dynamics and chemical reactions. Detailed modelling of this multi-physics process in turn requires a multi-scale approach to couple different physical phenomena. In this work, we model the leaking of LNG as a compressible multi-phase flow ignoring the effects of phase change and chemical reaction during the dispersion of leaked gases into the atmosphere. Details of the modelling approach are provided in the following sections.

2.1. Compressible Reynolds-averaged Navier–Stokes flow solver

CFD was used to model the process of gas leak in the form of jet or pool releases. It is assumed that the leaked gas combined with ambient air forms a mixture whose transport can be governed by compressible Reynolds average Navier–Stokes (RANS) equations (Wilcox, 2006) expressing the conservation of mass, momentum, and energy:

$$\frac{\partial \bar{\rho}}{\partial t} + \nabla \cdot (\bar{\rho}\tilde{\boldsymbol{u}}) = 0 \tag{1}$$

$$\frac{\partial \bar{\rho}\tilde{\boldsymbol{u}}}{\partial t} + \nabla \cdot (\bar{\rho}\tilde{\boldsymbol{u}}\tilde{\boldsymbol{u}}) = -\nabla \bar{p} + \nabla \cdot \boldsymbol{\tau}_{eff} + \bar{\rho}\boldsymbol{g} \tag{2}$$

$$\frac{\partial \bar{\rho}\tilde{h}}{\partial t} + \nabla \cdot (\bar{\rho}\tilde{\boldsymbol{u}}\tilde{h}) = \frac{D\bar{p}}{Dt} + \nabla \cdot (\boldsymbol{\alpha}_{eff}\tilde{h}) + S_h \tag{3}$$

In these equations, ρ is the density, $\boldsymbol{u}$ is the velocity vector, p is the pressure and h is the enthalpy; all of the mixture. The superscripts $\bar{()}$ and $\tilde{()}$ represent time-average and density-average quantities respectively in the framework of RANS simulations. For the sake of simplicity all the superscripts are dropped in the following equations. The effective stress tensor, $\boldsymbol{\tau}_{eff}$ is the summation of viscous and turbulent stress while α_{eff} is the effective thermal diffusivity. The transport of species in the domain is governed by the scalar transport equation

$$\frac{\partial \rho Y_i}{\partial t} + \nabla \cdot (\rho \boldsymbol{u} Y_i) = \nabla \cdot \left(\frac{\mu_t}{Sc_t}\nabla Y_i\right) + S_Y \tag{4}$$

where Y_i is the mass fraction of ith species where $\sum Y_i = 1$, μ_t is the turbulent viscosity of the mixture. Here Sc_t is the turbulent Schmidt number, $Sc_t = \mu_t/\rho D_m$ where D_m denoting mass diffusivity. In the above equations, S_h and S_Y are the source terms in the energy and species transport equations, respectively.

At the given length and time scale of the problem considered in this work, it is believed that the RANS approach provides sufficient resolution of turbulence quantities for the current simulations. In the context of gas dispersion, the realizable $k-\epsilon$ model has been shown to provide good resolution of turbulence transport (Luketa-Hanlin et al., 2007; Sun et al., 2013). The transport equations of turbulence kinetic energy and dissipation are described as:

$$\frac{\partial \rho k}{\partial t} + \nabla \cdot (\rho \boldsymbol{u} k) = P + B - \rho\epsilon + \nabla \cdot \left[(\mu + \frac{\mu_t}{\rho_k})\nabla k\right] \tag{5}$$

$$\frac{\partial \rho \epsilon}{\partial t} + \nabla \cdot (\rho \boldsymbol{u} \epsilon) = \nabla \cdot \left[(\mu + \frac{\mu_t}{\rho_k})\nabla \epsilon\right] + \frac{\epsilon}{k}(C_{\epsilon 1}P - C_{\epsilon 2}\rho\epsilon + C_{\epsilon 1}C_b B) \tag{6}$$

The production of turbulence by mean motion, $P = -\rho\overline{u_i' u_j'}\frac{\partial u_i'}{\partial x_j}$, is represented as a source term in both transport equations. B is the turbulence production due to buoyancy effect, $B = \frac{\mu_t}{\mathrm{Pr}_t}\frac{\partial \rho}{\partial x_i}\boldsymbol{g}_i$, where $\boldsymbol{g}$ is the gravitational coefficient vector. For jet release considered in this work the effects of buoyancy is neglected, unless otherwise specified as its impact is minimal compared with the convection and dispersion of high inertia gas plumes. The turbulent viscosity is computed from turbulent quantities as

$$\mu_t = C_\mu \rho k/\epsilon$$

The above model is implemented in OpenFOAM using existing numerical procedures available within the software framework. The velocity–pressure coupling is based on the pressure implicit with splitting of operators (PISO) algorithm. The compressible multi-species RANS solver will be used together with the realizable $k-\epsilon$ model for turbulence modelling. The model is closed with suitable initial and boundary conditions. In particular, the atmospheric boundary layer profile has been used in the project to initialize the wind profile. The roughness of the ground surface is also taken into account using wall functions.

Transient simulations of multispecies flows in this work were carried out using the unsteady solver with implicit second-order backward differencing scheme. There is a comprehensive range of spatial discretization schemes implemented in OpenFOAM, allowing full control over accuracy, boundedness and conservation. Here, a second order linear interpolation scheme was used for convective terms while a cell limiting scheme determining the limited gradient along a line connecting adjacent cell centres was used for the discretization of diffusive terms. Non-orthogonal and skewness correctors were also employed to maintain second order accuracy on unstructured grids. The use of implicit time stepping allows larger Courant number. For all the simulations in this work the Courant number is set to be 2.0, unless otherwise specified. The linear solvers of preconditioned conjugate gradient (PCG) and preconditioned bi-conjugate gradient (PBiCG) were used to solve the pressure and velocity respectively. Simplified diagonal based incomplete Cholesky (DIC) and LU (DILU) preconditioners were used in conjunction with the above linear solvers for pressure and velocity depending on the symmetry of the resulted linear system matrices. In addition, the turbulence equations were solved by the smooth solver in each step until a convergence tolerance was met. The convergence criterion of the simulations for all parameters was set to 10^{-6}, a value shown to give reasonably good convergent results from earlier experience.

2.2. Near field transient jet leak model

For LNG leaks, the release dynamics are rather complex due to the changing of phases during the process. Typically, when released to the ambient, LNG will vaporize and disperse into the environment. Depending on the storage and ambient conditions, some LNG remains in the liquid phase causing flashing of a mixture containing both liquid and gas. There are, therefore two approaches to model LNG release, namely, single-phase and two-phase.

In the two-phase model, flashing takes into account liquid drops ejected from the orifice and is typically concentrated near the release or leak point. In the single-phase model, it is assumed that LNG has fully vaporized when released from the orifice. The latter assumption is adopted in this work to model the jet leak of liquefied gas normally stored in super-heated states. However, it is noted that without taking into account the effect of flashing and rain-out, the current approach is limited in its predictability of liquefied gas in other storage conditions.

The leakage process is transient in nature. For a given leak condition, depending on the availability of various built-in safety measures, the characteristics of the leak scenario (such as leak rate, leaking duration, and the extent of gas cloud) can be unique. In this project, a transient leak tool was developed to model a typical LNG leaking process taking into account various safety procedures to determine a time-dependent leak rate. Typically, during this leaking process, the leak rate will reduce due to multiple reasons—depressurization in the pipe, the presence of safety mechanisms such as emergency shutdown devices (ESD) and blow-down system as required in most gas facilities. Upon detection of any possible leak utilizing a fire and gas detection system, the ESD valves will likely be activated, isolating the leak area. The dynamics of the leak rate will have to be modelled during four different stages: before detection, after detection, after isolation of ESD segments, and after initiation of a blow-down.

At every stage during the leakage process, the leak rate needs to be evaluated from the condition of gas/liquid at the leak location, including segment pressure, gas density among others. Depending on whether the flow is in the critical or sub-critical stages the leak rate will be determined accordingly, as

$$Q_{crit} = A \cdot C_d\sqrt{\rho_s p_s Z}\sqrt{\frac{2}{\gamma+1}^{\frac{\gamma+1}{\gamma-1}}} \tag{7}$$

or

$$Q_{subcrit} = A \cdot C_d\sqrt{2\rho_s p_s}\sqrt{\frac{\gamma}{\gamma+1}} \cdot \sqrt{\left(\frac{P_a}{p_s}\right)^{\frac{2}{\gamma}} - \left(\frac{P_a}{p_s}\right)^{\frac{\gamma+1}{\gamma}}} \tag{8}$$

In these expressions, p_s and ρ_s are the segment pressure and gas density in the leak area respectively while P_a is the ambient pressure

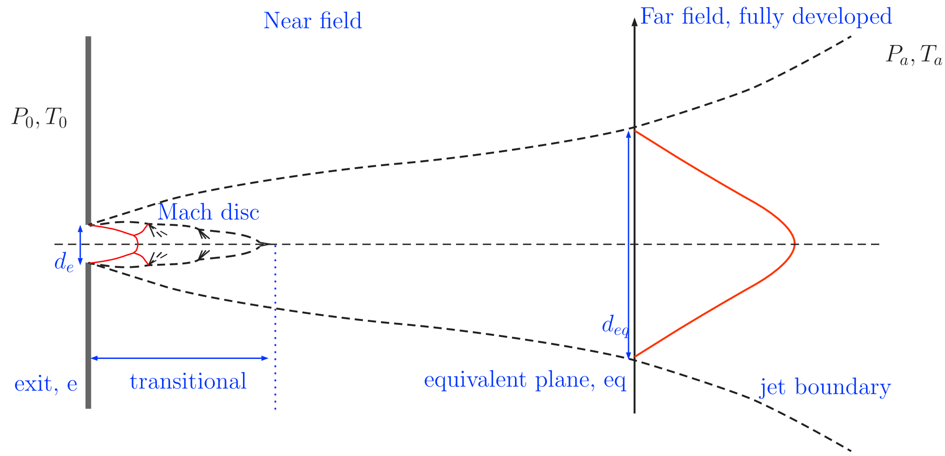

Fig. 1. Under-expanded jet regions with notions of near-field and far-field.

and γ is the heat specific ratio of the leaking gas. Here, C_d is normally referred to as the discharge coefficient taking into account the effects of contraction of the orifice. To a large extent, this empirical parameter of discharge coefficient takes into account other effects such as local curvatures in the orifice, viscous effects as well as real gas effects (Franquet et al., 2015). In this work C_d is taken to be 1.0 assuming that the leaking mass follows isentropic conditions of the ideal gas. From the above equations, a simple model is derived to determine the segment pressure and gas density from the remaining mass of gas compared to initial mass:

$$p_s(t) = p_{s,init}\frac{m(t)}{m_{init}}; \quad \rho_s(t) = \rho_{s,init}\frac{m(t)}{m_{init}} \tag{9}$$

The remaining mass of gas is computed from the initial mass and the leak rate as:

$$m(t) = m(t - \Delta t) + (Q_{in} - Q_{leak})\Delta t \tag{10}$$

In the above expression, Q_{in} is the inflow mass rate and Q_{leak} is the mass flow rate of the leak. The input flow rate is related to the flow rate in different sectors of the bunkering pipeline. The leak flow rate is evaluated from Eqs. (7)–(8) depending on the flow regimes. It is assumed that the leak rate before detection is constant for small leakages. When the safety processes activate prior to isolation, there will be a gradual reduction in the inflow flow rate from an initial value to close to no flow. The leak flow rate also decreases when the segment pressure is reduced during the leaking process.

After exiting the orifice from a highly pressurized state, the liquefied gas normally under-expands to the ambient condition. Fig. 1 depicts a typical flow structure in the near-field region close to the orifice, composed of normal shocks and their reflections causing Mach discs with a triple point. As highlighted previously, including the modelling of the near-field region greatly increases the computational cost and time. Hence in this work, a pseudo-source model is adopted from literature (Franquet et al., 2015) to compute the equivalent flow conditions in the far-field region when exiting the orifice. Essentially in the pseudo-source or notional nozzle model, it is assumed that the jet that started from the exit plane and expanded to the far-field region is replaced by an equivalent flow whose conditions are specified by the stagnation and far-field states (e.g.: pressure, temperature). To take into account the depressurization of the gas as well as decay of the jet, the equivalent flow condition is specified at an equivalent diameter for maintaining the conservation of mass, momentum, and possibly energy. Assuming that the equivalent flow is depressurized to ambient pressure ($p_{eq} = P_a$) while its temperature is equal to the stagnation temperature ($T_{eq} = T_0$), the equivalent diameter and velocity can be computed as:

$$\frac{d_{eq}}{d_e} = \sqrt{\frac{V_e \rho_e}{V_{eq}\rho_{eq}}}, \tag{11}$$

$$V_{eq} = V_e + \frac{p_e - P_a}{V_e \rho_e}. \tag{12}$$

In the above expressions, V denotes the jet velocity, subscripts e and eq refer to the exit and equivalent conditions, respectively. The exit velocity and the pressure can be determined from the stagnation condition and the size of the orifice (d_e) as well as the gas thermodynamic properties. For a perfect gas and assuming a choke condition at the exit plane, the equivalent diameter can be expressed as a function of pressure ratio $\eta_0 = P_0/P_a$ as (Franquet et al., 2015):

$$\frac{d_{eq}}{d_e} = \sqrt{\frac{\gamma}{\gamma+1}\left(\frac{2}{\gamma+1}\right)^{1/(\gamma-1)}\eta_0}, \tag{13}$$

where P_0 is the stagnation pressure in the tank.

Fig. 2 shows the transient profiles of storage and equivalent conditions resulted from a leak experiment of supercritical methane (Ruffin et al., 1996). In this experiment, the methane gas stored at $40 bar$ and $288K$ was released from a pressurized tank of volume $5m^3$ into atmospheric conditions through an orifice of diameter 25 mm. At the given release condition, the equivalent release condition can be obtained using different equivalent diameter models as shown in Table 1. Coupling the equivalent diameter models with the earlier transient process of leaking provides a complete description of a jet leak from an orifice at any given condition as shown in Fig. 2. From the figure it can be seen that the current model depicts the reduction in tank pressure and leak rate as the gas was released through the orifice. It takes about 150 seconds for the tank to become empty and the equivalent conditions of the jet can be computed to provide boundary conditions for CFD simulations subsequently. The transient leak profiles can be incorporated into the CFD solver as a time-varying boundary condition for subsequent far-field simulations of the gas dispersion process.

2.3. Numerical validation

For verification and validation purposes, we used the previously proposed approach for a numerical experiment of methane jet leak following the earlier physical test (Ruffin et al., 1996). In this set-up, supercritical methane stored at a pressure of 40 bar and temperature of 288K was released from an orifice of diameter 25 mm to atmospheric condition. The volume of the gas in the tank was $5m^3$ and the leak location was 5m above the ground, mirroring the experimental setup. The computational domain and boundary conditions for the simulation are shown in Fig. 3. Here, a neutral class atmospheric boundary layer condition (ABL) is prescribed at the inlet while the outlet pressure boundary condition is applied at the downstream boundary. The wind speed at the inlet are given by Huser et al. (1997)

$$\frac{u(z)}{u^*} = \frac{1}{\kappa}\left(\ln(\frac{z}{z_0}) - \Phi_M(\frac{z}{L}) + \Phi_M(\frac{z_0}{L})\right) \tag{14}$$

Table 1
Equivalent leak conditions using different models for a jet leak of 25 mm in diameter from a reservoir of 40 bar, 288.0 K to ambient environment at 1 bar, 298 K.

Model	Sonic Jet	Pseudo-diameter	Improved PD	Equivalent
Equivalent diameter (m)	0.1168	0.1219	0.0742	0.0742
Pressure (Pa)	1.0E5	1.0E5	1.0E5	1.0E5
Temperature (K)	250.43	298.0	175.05	275.51
Velocity (m/s)	411.30	448.67	713.20	237.20
Density (kg/m^3)	0.7684	0.6458	1.0994	3.3055

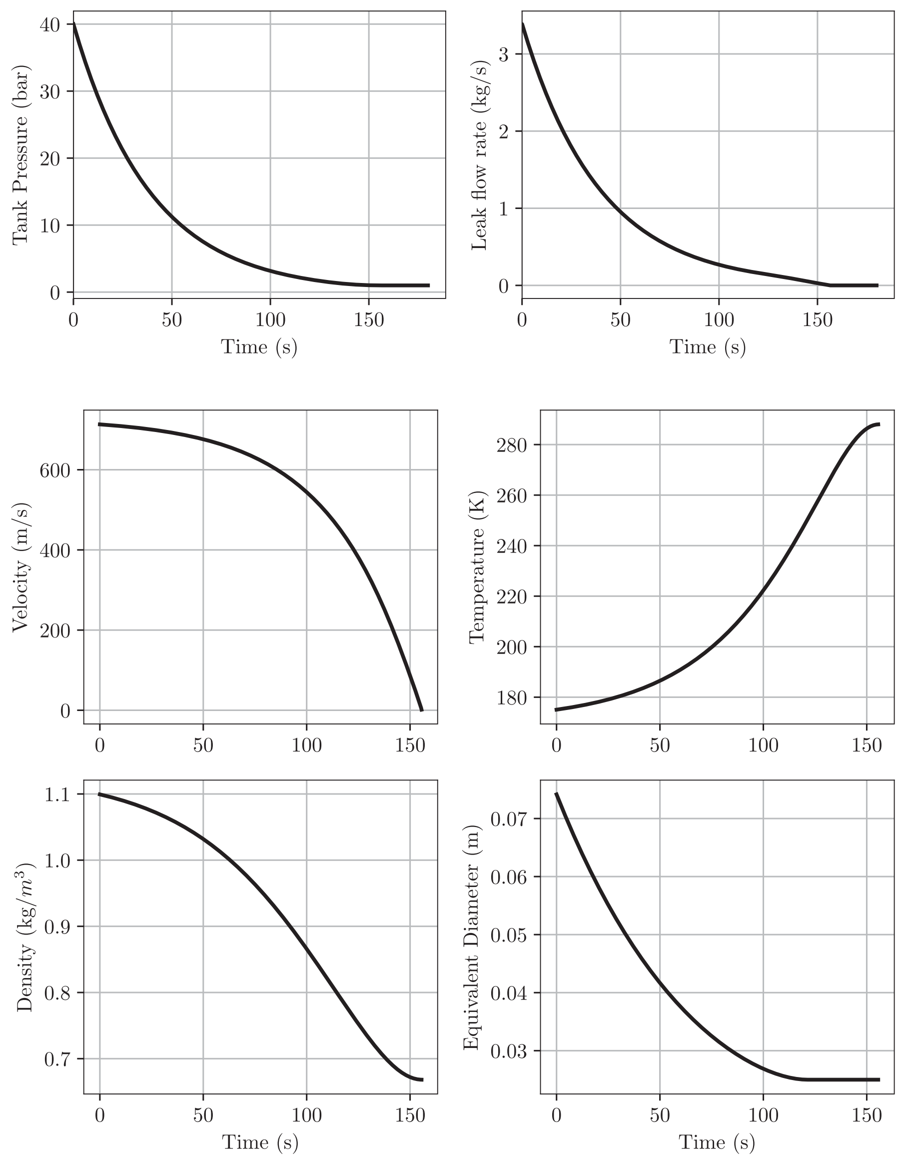

Fig. 2. Transient leak profiles in the tank and at the equivalent condition for a leak from a tank of supercritical methane gas at 40 bar and 288K through an orifice of 25 mm using improved pseudo-diameter model. The initial conditions are taken from the experiment (Ruffin et al., 1996) and used for validation of numerical model.

where u^* is the friction velocity, κ denotes the von Karman's constant equal to 0.41, z_0 is surface roughness length parameter, L indicates the Monin–Obunkhov length and $\Phi_M = -17\left(1 - e^{0.29(z/L)}\right)$. The friction velocity can be calculated from a given speed at a reference height. The surface roughness varies between different types of terrains and typologies, here we use $z_0 = 0.035$ for flat terrain in all simulations, except otherwise specified. Other quantities including temperature and turbulent kinetic energy, dissipation rate can be similarly described at the inlet following the same procedure shown in Huser et al. (1997).

The grid is a regular structured grid and controlled by a background grid resolution (Δx_{max}) with further grid refinement around the leak location. Resolution of the grid in this region is determined by a number of refinement levels. Each subsequent refinement level halves the cell size of the selected cells. It is worth noting on the importance of consistently maintaining ABL profile up to the domain of interest and different approaches proposed in literature Parente et al. (2011) to ensure consistency of the ABL profiles. In this work, we designed the grid with consistent vertical spacing and stretching throughout the domain to make sure ABL conditions are consistently propagated into the domain. From our observation the velocity may experience deflection of profiles, TKE and dissipation rate are consistently maintained with the use of the above design grid. As the current problem focuses more

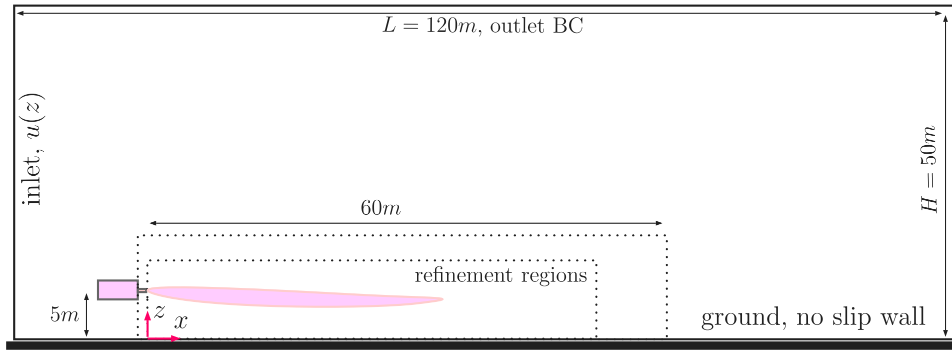

Fig. 3. Computational domain and boundary conditions for the numerical experiment of leaking supercritical methane into the atmosphere (outlet, where P_a indicates atmospheric pressure). The domain includes the refinement regions around the leak location where mesh resolution can be changed by successive refinements. Note that the tank and nozzle geometries are not present in simulations.

Table 2
Grid convergence results for simulations of supercritical methane leak with changing mesh resolution. Here, the grid convergence index (GCI) is computed from CH_4 profiles as $GCI_{grid_i} = \frac{|f^{CH_4}_{G_i} - f^{CH_4}_{G_{i-1}}|_{L_2}}{|f^{CH_4}_{G_{i-1}}|_{L_2}}$.

Grid	Δx_{min} (m)	Δx_{max} (m)	Refinement Ratio	GCI (%)
G0-coarse	0.200	10.00	–	–
G1-base	0.100	10.00	2.0	2.45
G2-fine	0.050	10.00	2.0	8.22
G3-finest	0.025	10.00	2.0	1.02

on near-field dispersion from a jet release and confined in a smaller domain (< 100m) we believe the effect due to the above deflection of ABL profiles is small. For pool releases (due to evaporation) into atmosphere this effect is more significant and it requires a modification to the turbulence model (Parente et al., 2011) to ensure consistency of ABL profile.

Fig. 4 shows the comparison of methane concentration between numerical simulations and experimental measurement along the centre line from the orifice in the downstream direction for different mesh resolutions and transient leak models as shown in Table 1. Using the improved pseudo-diameter transient leak model, the numerical prediction of methane concentration along the centre line best matches the experimental data with finer grid resolution as seen in Fig. 4a. In Table 2, the sensitivity of concentration profiles to successive grid refinement demonstrated the convergence of numerical prediction with changing grid resolution. At the finest grid level, the convergence index reaches an acceptable range of 1% with the grid resolution of $\Delta x = 0.025$m, about the same as the original leak diameter. Simulations were next carried out with different transient leak models on the same grid level. Results of methane concentration along the centreline shown in Fig. 4b indicate that the improved pseudo-diameter model outperformed other approaches in the prediction of the plume spread. In the subsequent analysis we adopt this improved pseudo-diameter and grid resolution of at least one cell per leak diameter for all the simulations.

3. Simulation of gas cloud dispersion from LNG jet leaks

In this section, the numerical model was applied for simulations of different leak scenarios from a mock-up LNG bunkering station. The station geometry was obtained by simplifying the existing facility that includes main pipes, a base frame, supporting structures, and an enclosure. Assessing the spread of gas cloud from keyhole leakages during the bunkering process is required in a risk assessment procedure for the design and operation of this type of facility.

3.1. Problem set-up

One of the most significant events during LNG bunkering is the keyhole leak from the hose. Keyhole leaks are considered less likely with low probability; however, they pose a great risk to the operation. Specifically, we consider a typical leak condition due to a hose/pipe fracture with the representative leak diameter of $d_{leak} = 25$ mm from a pipe of diameter $D_{pipe} = 200$ mm and a section length of $L_{pipe} = 10m$. The LNG with methane as the main component is normally stored at the condition of pressure $P_0 = 10bar$ and temperature of $T_0 = 112K$. The leak and pipe diameters are taken from a common specification in LNG transfer and recommendation of the risk assessment procedure (Anon, 2016; Society for Gas as a Marine Fuel, 2018). The pipe length is specified as the maximum distance from a leak location to the closest ESD valve.

The wind condition is in the range of very low wind speeds $U_0^{min} = 0.1$ m/s to strong wind speeds of $U_0^{max} = 7.72$ m/s. Here we chose the maximum wind speed according to the recommended wind speed allowed for bunkering operation in the Singapore yard of 15 knots or about 7.72 m/s. It is assumed that the north wind direction is aligned with the bunkering station. The computational domain and a typical grid topology are shown in Fig. 5 for simulations of gas cloud dispersion from an accidental key hole leak event. In order to resolve the effect of those geometrical features during leakage, a hexahedral-dominant unstructured grid was generated for the computational domain as seen in Fig. 5. Mesh refinement is performed in the region of interest and around the enclosure. The grid is further refined around the geometrical features to better resolve their complex shapes and topologies. At the leak location, the grid is at the finest refinement level to ensure the resolution of at least 1 cell per leak diameter as recommended from the earlier grid convergence study.

The neutral ABL inlet and pressure outlet boundary conditions described in the earlier section are applied at the corresponding boundaries of the computational domain, depending on the wind direction. No slip boundary condition is applied at the walls on the enclosure, pipes and frame. Transient simulation was initiated for LNG leakage with initial condition of flow fields (velocity, pressure and temperature) obtained from the steady state simulation of the same wind condition. The transient leak profile obtained from the near-field jet leak model is prescribed at the leak location for flow rate and temperature. All simulations were performed until the flammable cloud reaches a maximum distance or the tank is empty.

3.2. Analysis of gas clouds

In this section, we consider two prevailing wind directions in Singapore, namely, the North–North East and the South wind (win) at the speed of 7.72 m/s (i.e. 15 knots) measured at the reference height

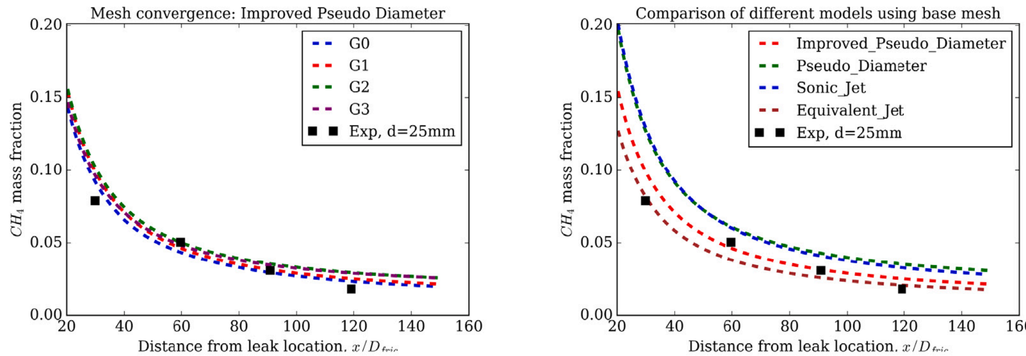

(a) mesh sensitivity (b) sensitivity with leak model

Fig. 4. Gas plume concentration along the centreline of the domain from a leak through orifice of 25 mm diameter with different mesh resolutions and transient leak models. Results are compared with experimental data (Ruffin et al., 1996).

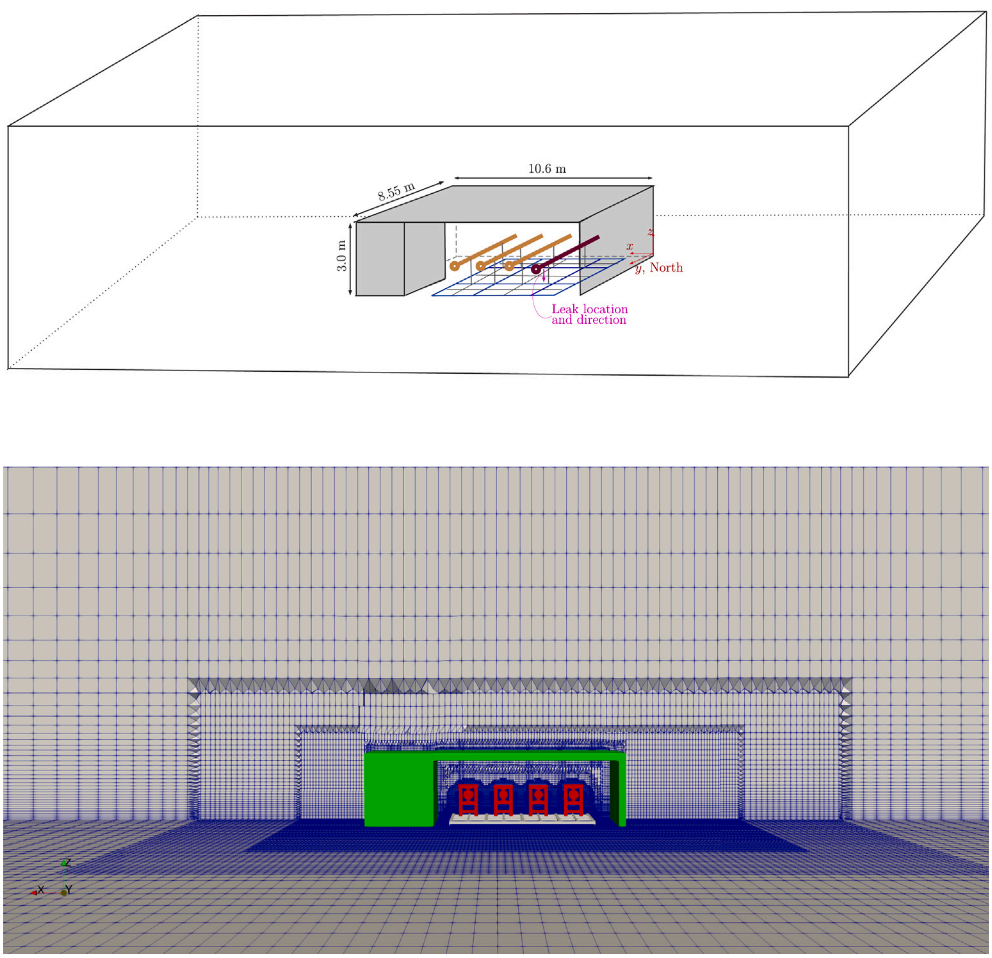

Fig. 5. Computational domain of bunkering station with enclosure showing basic dimensions of the configuration considered in the present work. Leak is initiated from the right most pipe in the manifold at 1.1 m from the ground in downward direction.

of 10 m. Fig. 6 shows methane volume fraction distribution within the enclosure for the case of the north wind. It is observed that a cloud of methane accumulates at the rear of the enclosure and spreads due to complex interaction with surrounding obstacles. This cloud is formed by the methane jet leak impinging on the drip tray, travelling to the rear along the tray, deflecting upwards by the base frame, and finally deflecting downwards by the enclosure ceiling. It is also noted that there are significant regions at the rear of the enclosure that are free of methane. The rear of the enclosure directly below the ceiling may, therefore, be a good location for suction fans or other ventilation facilities for mitigation planning.

Results from the simulation for the north wind direction are shown in Fig. 7 for the isosurfaces of lower flammable limit (LFL) concentration ($\alpha_{CH_4} \geq 5\%$). The LFL methane gas plumes are spread within the enclosure as well as dispersed outside the enclosure. Due to the effects of the wind, the gas clouds grow larger and away from the centre of the leak before reaching a maximum length. When the leak rate is reduced

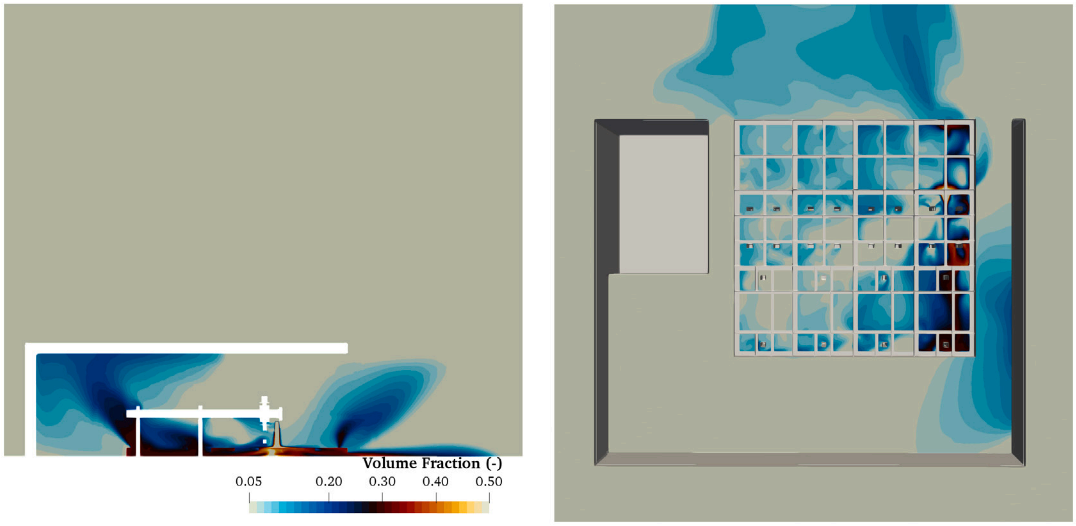

(a) x=0.72 m

(b) z=0.0045 m

Fig. 6. Regions where methane volume fraction is above LFL are shown on cut planes at (a) $x = 0.72$ m and (b) $z = -0.0045$ m with reference to the origin placed on the right corner of the enclosure as shown in Fig. 5. The plane at $x = 0.72$ m intersects the liquid line at the location of the leak, the plane at $z = -0.0045$ m intersects the base frame. These plots are for the case of north wind of 7.72 m/s at $t = 7.5$ s.

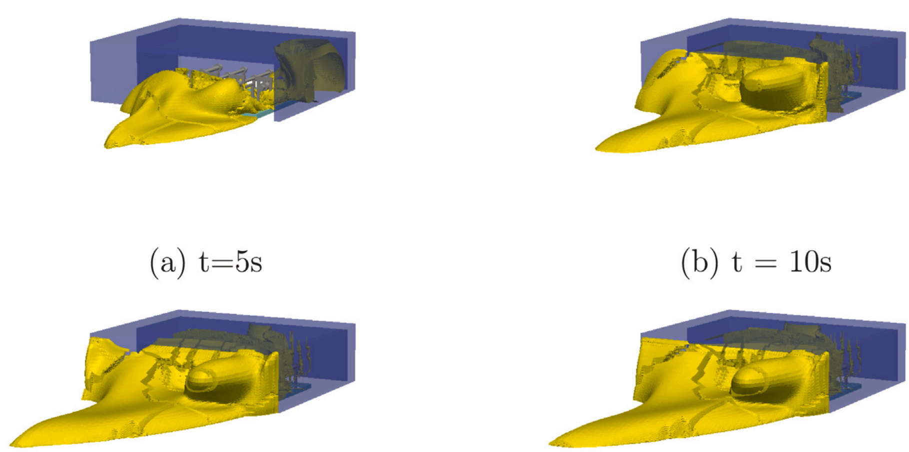

(a) t=5s

(b) t = 10s

(c) t=12.5s

(d) t = 15s

Fig. 7. Transient gas plume from the key hole leak under strong wind condition of $U = 7.72$ m/s from north direction. It is noted that the LFL cloud grows with time and reaches its maximum spread before being retracted due to dispersion.

further, it is expected that the gas clouds retract and become smaller due to the effects of the wind.

Fig. 8 depicts an instantaneous LFL cloud of methane at 7.5 s from start of the leak for two prevailing wind directions. It can be seen that the wind direction affects spreading of the gas cloud coupled with the effects of surrounding obstacles such as the enclosure; north wind blows air into the enclosure. For the south wind, the methane gas cloud tends to spread faster and further downstream compared to the case with the north wind. Due to the blockage of the enclosure, the north wind tends to hold the cloud from spreading southwards. This is intuitive as the enclosure is designed with a big north-facing opening for bunkering operations thus countering the north wind at the same time. Fig. 9 shows spreading of the LFL gas cloud with time for different wind directions. The spread distance is measured as the distance of the farthest points of the LFL cloud to the leak centre. The maximum spread of the LFL cloud can reach beyond 40 m and it is strongly dependent on the wind direction. It can be seen that the enclosure has effectively limited the spread of LFL gas for the northern wind.

Fig. 10 shows the contours of LFL residence time in the domain for different wind directions. The LFL residence time, τ measures the integrated duration of LFL clouds present at a location throughout the leaking process as

$$\tau(\mathbf{x}) = \int_{t=0}^{T_\infty} I(x)dt, \tag{15}$$

where $I(x)$ is the indicator if methane gas concentration is above the LFL at a location:

$$I(x) = \begin{cases} 1, & \alpha_{CH_4} \geq 0.05; \\ 0, & \text{otherwise.} \end{cases} \tag{16}$$

Here α_{CH_4} is the volume fraction of methane computed from the mass fraction. The lower flammability limit (LFL) has been used throughout

(a) north wind (b) south wind

Fig. 8. Gas plumes from key hole leak in a bunkering station with different wind direction. The cloud shapes are shown at $t = 7.5$ s after the onset of leakage.

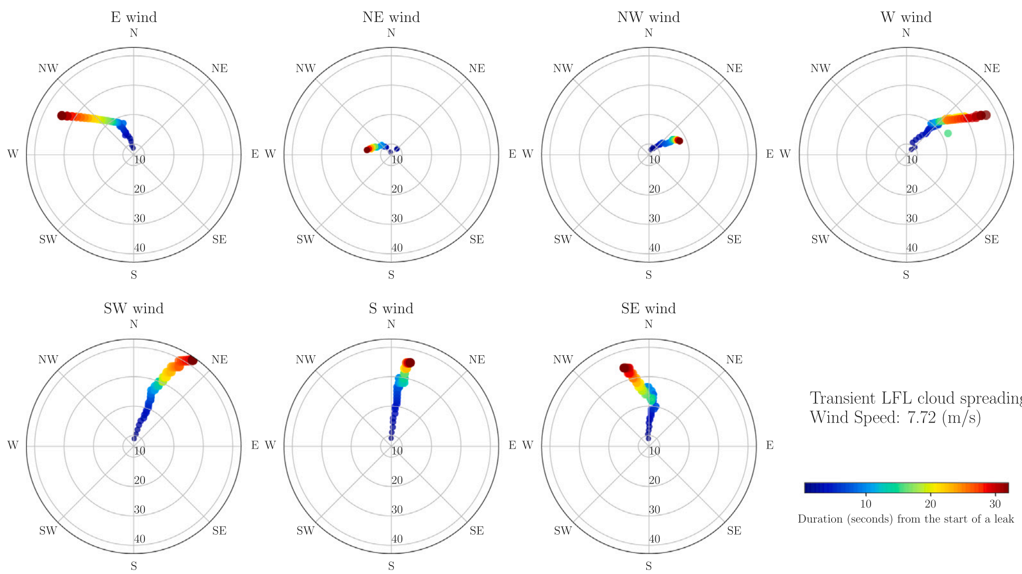

Fig. 9. Transient LFL gas cloud spread distance and angle for different wind directions. The spread distance is measured from the tip of the cloud to the leak centre. The spread distance increases with time until reaching the maximum distance, limited by the computational domain.

this work to mark the front flammable surface of the gas plumes. While it does not depict a strictly flammable zone between LFL and UFL (upper flammable limit), it provides a good estimation for the spread of LNG from a leak. In Fig. 10, the residence time is spatially averaged along the vertical direction from the ground up to 20 m above the ground. From the presented result, the residence time consistently shows that the north side of the enclosure is highly likely exposed to LFL methane than the south side which is sheltered by the enclosure. The vertical average of residence time can also be used to access the spatial exposure to the hazardous gas cloud, thus assisting the design and spatial planning of supporting facilities in the immediate vicinity of the bunkering station.

4. Uncertainty quantification using polynomial chaos expansion

From the preceding figures, it is clear that changes in the wind direction strongly influence the spread of gas plumes. Along with wind speed and direction, there are many other parameters that play an important role in the risk assessment of bunkering facilities. These include operational parameters (storage pressure, temperature) and leak conditions (keyhole leak diameter, location, leak direction), among others. Among those parameters, uncertainty in the wind conditions is considered in this work to investigate its impact on plumes' spreading and safety distance in the event of keyhole leaks. Generally, the output quantities of interest (such as gas plume spread distance, angle or LFL residence time) depend on these uncertain inputs as

$$\mathbf{y} = \mathsf{f}(\mathbf{x}, t; \mathbf{q}), \tag{17}$$

where $\mathbf{y}$ represents the output of interest and $\mathbf{q}$ represents the uncertain inputs, x and t represent the variation of the output function with space and time. Forward model f provides a response of the system to changes in inputs. It is assumed that uncertainty of the input is known with a probability distribution function $_{\mathbf{q}}$ in this case. The main goal in the uncertainty quantification process is to find a distribution of the output $_{\mathbf{y}}$ with the given input uncertainty.

4.1. Uncertainty in wind conditions

Fig. 11(a) shows the average annual windrose data in Singapore (win) reflecting two dominant wind directions from the north-north east and south directions. The dominant wind directions are strongly influenced by two monsoon seasons in Singapore, in which the northerly and northeasterly winds are stronger during Northeast monsoon. Data from the windrose can be sampled into a distribution for wind speed and direction as shown in Fig. 11(b). The probability density function (PDF) clearly indicates a bimodal distribution of the wind direction. The sampled PDFs are then approximated by a bimodal and gamma distribution for wind direction and speed respectively. This approximate distribution is subsequently used as an input to quantify impacts of the uncertainty of wind conditions on gas dispersion.

4.2. Decoupled CFD approach for faster simulations of jet leak gas dispersion

The current simulation approach for simulation of jet leaks uses a single computational domain that includes the geometry (pipes and enclosure) along with the open space representing the surroundings and ambient. As a fine mesh resolution is needed near the leak, this typically results in a larger mesh count for the entire domain to ensure

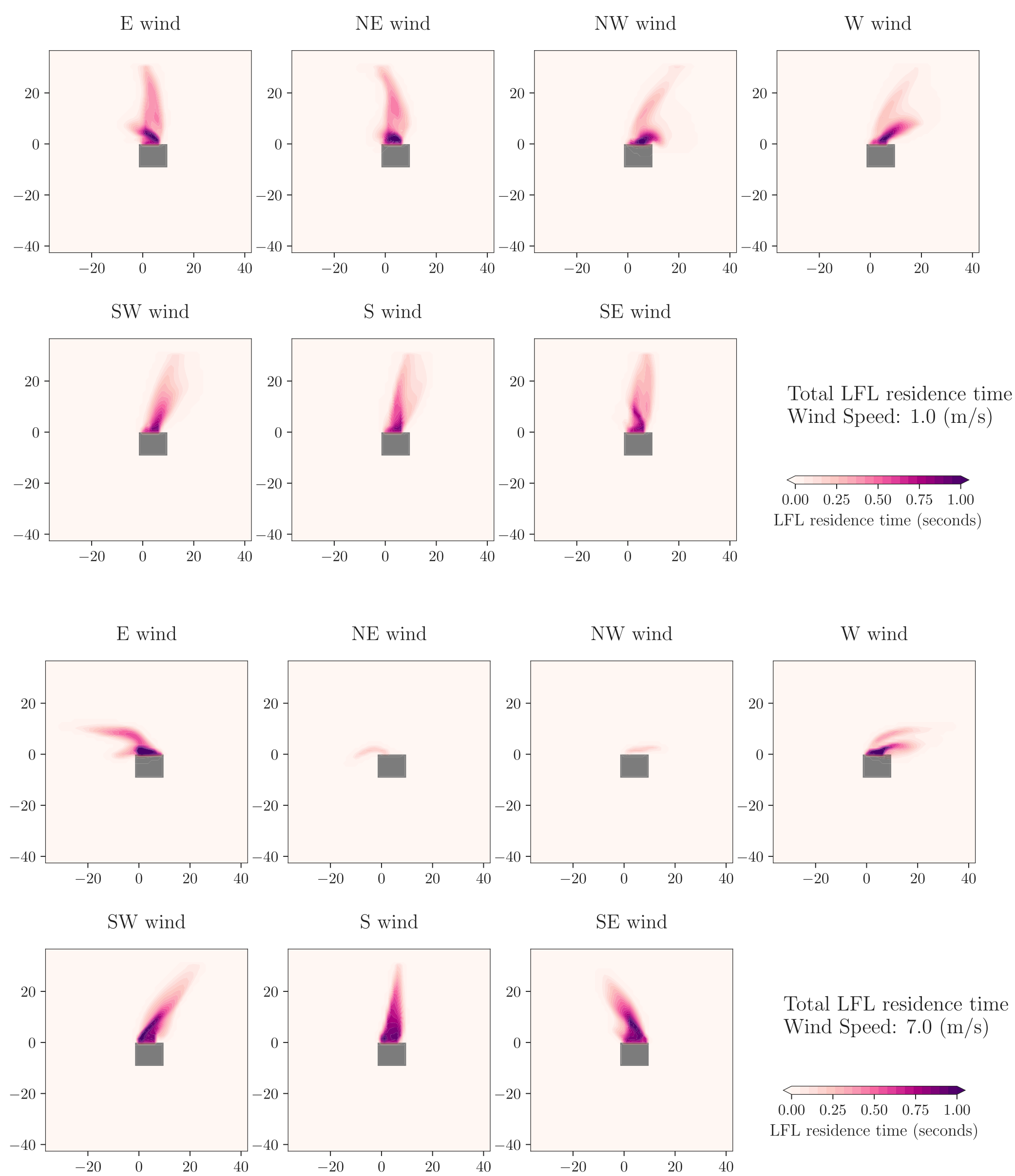

Fig. 10. Vertically averaged residence time of LFL of methane gas for different wind directions for different wind speeds. It measures the duration of presence of LFL of gas in space providing information on hazardous exposure.

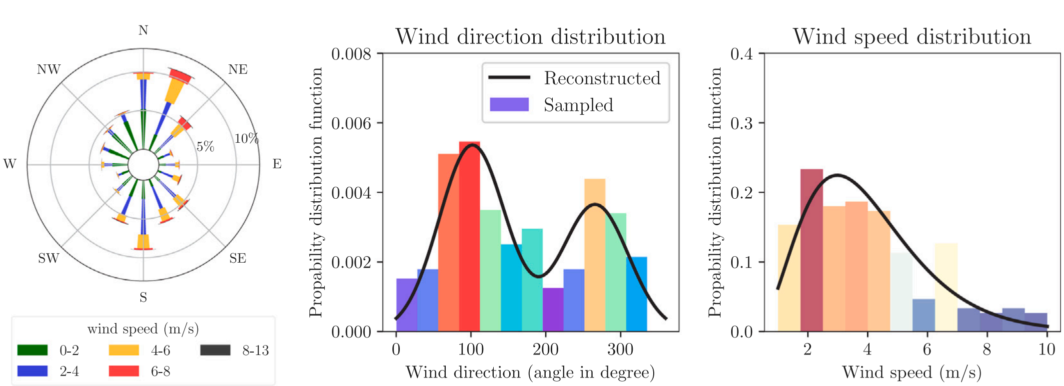

Fig. 11. Left: annual windrose of Singapore (1981–2010) (win) and right: the derived distribution of wind conditions. In the distribution of wind speed and direction, the bars show distribution sampled from windrose data and the solid line is the approximate distribution.

sufficient transition of grid resolution across the domain from the leak centre. Performing simulations for different wind conditions on this large mesh for the whole domain is time consuming, especially when a large number of scenarios need to be considered during the design exploration or uncertainty quantification stages. In such situations, models and solutions that have reasonably short run-times while also providing qualitative information would be more suitable.

With this in mind, a decoupled approach was explored for the leak simulations. The idea behind the decoupled approach was to first create two separated sub-domains from the whole computational domain. One of the sub-domains represents the external, while the other represents the inside of the enclosure. In this decoupled approach, the internal sub-domain comprises the enclosure and other internal structures (pipes, base). The external domain is coupled with internal one via the interface which transfers information from the internal to the external domain using a time-varying boundary condition. For the current case, the front opening of the enclosure was taken as the interface boundary of the two domains. It is assumed that wind conditions have minimal impact on internal flows in the enclosure. This is a reasonable assumption when the direction of the wind is not blowing into the enclosure. Simulations of flows in the internal domain comprising of the geometry and the leak are first performed under a no-wind scenario. The values at the opening of the enclosure from the internal domain are stored and are used as "source" values for the external domain simulations. The external domain comprising of the enclosure (as a solid mass) and the rest of the domain is considered subsequently. For the external domain, different wind scenarios (speed and direction) can be simulated with the same input from the internal sub-domain at a specified leak condition.

In this manner, the internal domain requires only a single run for each leak condition. The external domain, in the absence of geometrical features that require finer mesh resolution, can have a smaller mesh count and consequently runs faster. Fig. 12 shows the instantaneous flammable clouds obtained from the decoupled approach in comparison with the fully coupled simulation at different time stamps. In this comparison, the two simulations are performed on the exact same external mesh resolution. From the prediction of the cloud spreading, the cloud extent and shape obtained from the decoupled simulation are very similar to the fully coupled simulation with some small differences. It can be seen that closer to the opening of the enclosure, the decoupled approach tends to over-predict the cloud spreading as the coupled effects of internal features from inside the enclosure are not present. With the input of solution on the domain interface obtained from the coupled simulation, the decoupled prediction shows good agreement with the coupled one for velocity and cloud spreading as shown in Fig. 12. Furthermore, it is also worth noting that the decoupled approach takes much less time to run compared to the fully coupled simulation. On a workstation of 28 cores and 256 GB of memory, a decoupled simulation takes about 40–50 times less than the coupled one for the same wind condition with the same mesh resolution. Despite its shortcoming in accuracy, the decoupled approach gives a qualitative picture of which of the wind scenarios is the worst-case scenario for the current design as was seen in Fig. 9. Based on this quickened analysis, the more detailed and quantitative simulation (using the single domain approach) can be performed to better understand the plume spread.

4.3. *Reduced order forward model for gas dispersion*

Generally, uncertainty quantification requires a forward model to propagate input uncertainties to the output. The earlier presented CFD approach is capable of evaluating output responses for a random input; however, the CFD evaluation is computationally expensive, in particular for a given large number of samples in the input parameter space. This remains the case even with the decoupled approach, which while quick is still not fast enough to be able to perform hundreds of simulations quickly. In such cases, it is essential to approximate the full CFD model responses using surrogate models. In this work, we propose to build a reduced-order model (ROM) as an approximation to CFD evaluation. There exists a wide range of model reduction techniques in the literature Chinesta et al. (2017). Essentially, a ROM is developed to obtain low-dimensional approximate descriptions of high-dimensional processes. For instance, in this work, the volume fraction of methane and the LFL residence time field can be approximated in a reduced space as

$$\alpha_r(\mathbf{x};q) = \sum_{i=1}^{N_u} a_i(q)\phi_i(\mathbf{x}); \quad \tau_r(\mathbf{x};q) = \sum_{j=1}^{N_p} b_j(w)\psi_j(\mathbf{x}) \tag{18}$$

where ϕ_i and ψ_j are the spatial reduced basis vector for volume fraction and LFL residence time approximation space respectively. In the above expression a and b are the weighting coefficients associated with the corresponding basis vectors or modes. Proper orthogonal decomposition (POD) is the most common technique in providing spatial modes for low-dimensional representation of high-dimensional system states. Here we implemented a ROM based on POD with parametric interpolation (PODI) approach as a forward model for uncertainty quantification.

In a nutshell, the PODI approach consists of two stages. First, in the offline stage, full-order or high fidelity solutions are computed and stored in a snapshot matrix for different design parameters:

$$\mathbf{S} = \left\{\mathbf{U}_{h,1}, \mathbf{U}_{h,2}, \ldots, \mathbf{U}_{h,N_s}\right\} \tag{19}$$

where $\mathbf{U}_{h,i} \equiv \mathbf{U}(\mathbf{x};q_i)$ is the high fidelity solution at parameter q_i. The spatial modes in a reduced basis can then be computed through POD using the method of snapshots (Chinesta et al., 2017). Subsequently, the high fidelity solutions are projected back into POD modes to obtain modal coefficients. In the second stage of the PODI approach, the online phase, the modal coefficients are interpolated for any new design parameters and the corresponding solution can be approximated in a reduced order space. For more information on PODI, one can refer to the review in Chinesta et al. (2017) and the references cited therein. With the pre-computed POD modes and fast interpolation of modal coefficients, the online stage normally takes a fraction of time compared to the high fidelity model, thus making it ideally suitable for uncertainty quantification.

A database for PODI approach was built by running the high fidelity CFD model on 40 samples using Latin hypercube sampling technique (Adams et al., 2014). Fig. 13 shows the scatter plot of plume spread distance and angle for the sampled wind conditions. The sampled dataset is divided into training and testing subsets for building a PODI model. The training set of CFD solutions was used as offline data. Fig. 14 shows the snapshots of POD modes obtained from 24 CFD samples together with their corresponding eigenvalues. Those POD modes were then used for interpolation of a solution to a new wind condition in the test dataset as shown in Fig. 15. It is worth noting that predictions from the PODI show very similar LFL residence contours compared to CFD results. In Fig. 16, the error between POD prediction and CFD solutions are shown for training (projection) and testing (interpolation). It can be seen that the projection errors are significantly small compared to the interpolation errors reflecting the intrinsic property of POD in minimizing projection errors. It is also known that POD interpolation is sensitive to the size of the dataset. Table 3 depicts the mean and standard deviation of the projection and interpolation errors obtained from PODI with a variation of the number of snapshots used for POD. By varying the number of snapshots (training subset) from 50%–80% of the total number of samples, the mean and standard deviation of the errors do not vary much; showing the independence of POD predictions on the size of snapshots.

4.4. *Polynomial chaos expansion (PCE)*

A non-intrusive PCE is used in this work to propagate the randomness of inputs through the forward model to quantify the output responses. In a typical uncertainty quantification process, the statistical

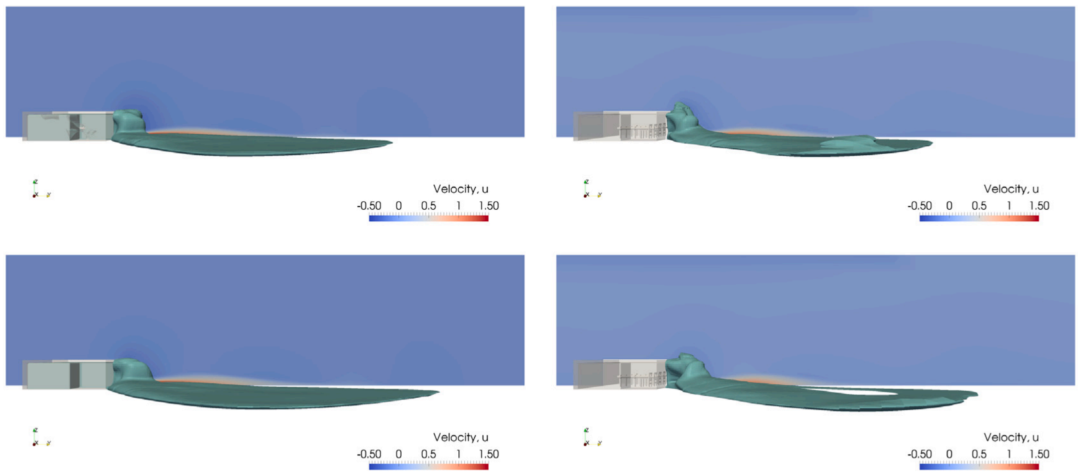

Fig. 12. Comparison of instantaneous velocity profile and flammable LNG clouds obtained from decoupled (right) and coupled (left) approach for the low wind condition. Top and bottom panels are results at time $t = 15$, 20 s, respectively.

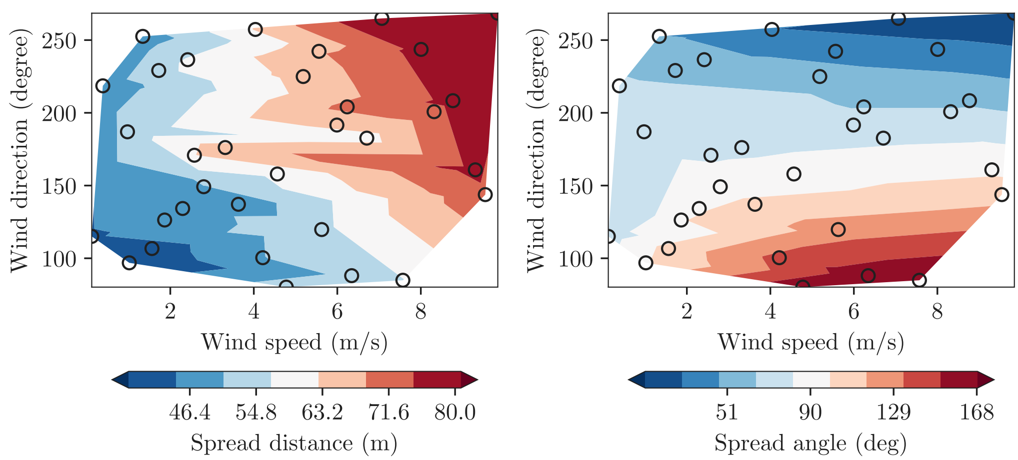

Fig. 13. Scatter plot of maximum spread distance and angle of methane gas cloud for the sampled wind conditions used as offline snapshot in PODI process.

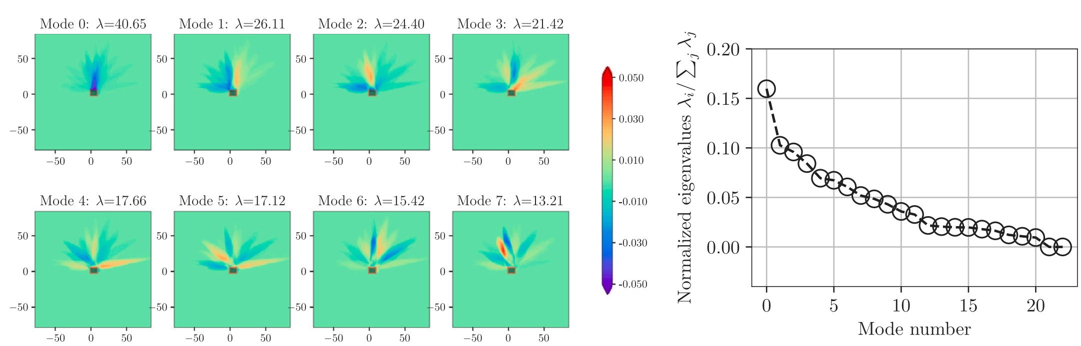

Fig. 14. POD modes (left) and eigenvalues (right) of LFL residence time obtained from samples of 24 snapshots (60% of the total sampled data).

properties of the output function y such as the mean μ_y and the variance σ_y^2 are sought as

$$\mu_f = \int \mathscr{F}(\mathbf{q})(\mathbf{q})dq, \qquad \sigma_f^2 = \int (\mathscr{F}(\mathbf{q}) - \mu_f)^2(\mathbf{q})dq. \tag{20}$$

Here $\mathscr{F}(\mathbf{q})$ is the stochastic output function of a random input. In the generalized polynomial chaos (gPC) (Xiu, 2009) expansion, the stochastic output can be expressed as an orthogonal polynomial approximation of random input parameters as

$$\mathscr{F}_{PCE}(\mathbf{q}) \approx \sum_{j=0}^{n} \lambda_j \phi_j \tag{21}$$

where $\boldsymbol{\phi} = \{\phi_0(.), \phi_1(.), \ldots, \phi_n(.)\}$ is the polynomial basis function and λ_j is the weighting coefficient. For a given smooth distribution of input parameters, it has been shown that exponential convergence can be achieved with suitable orthogonal polynomials similar to a spectral representation of the output function in random space (Xiu,

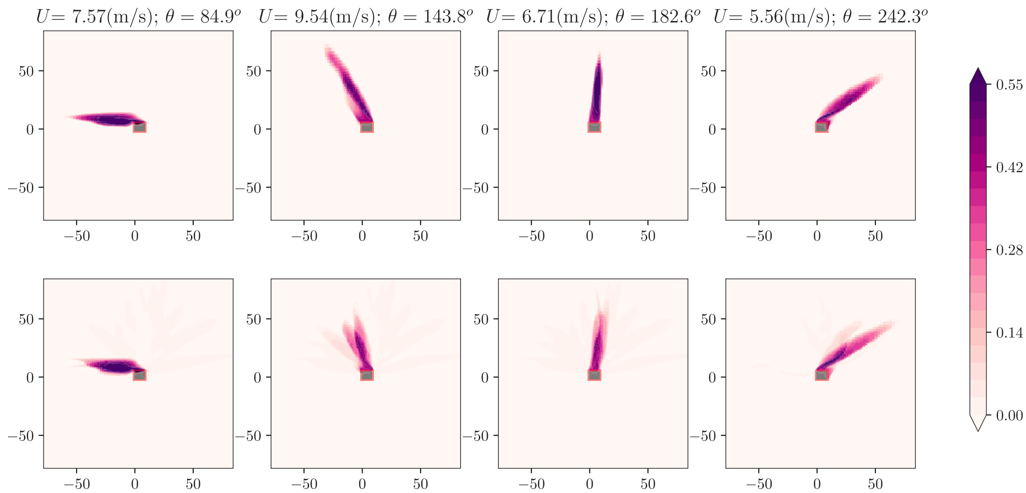

Fig. 15. POD interpolation of LFL residence time (bottom panels) with CFD solutions (top panels) for different wind conditions in comparison.

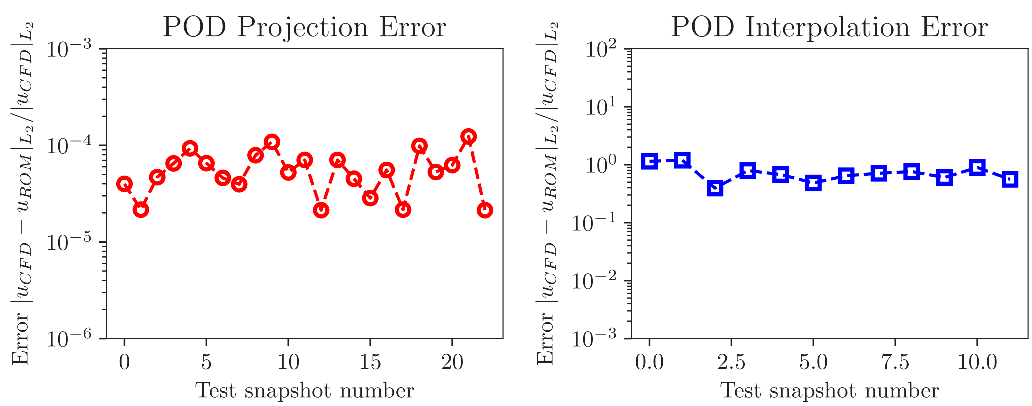

Fig. 16. Projection and interpolation errors between CFD and PODI using 24 snapshots for POD modes. The normalized error is measured as L_2 norm error between POD prediction and CFD solutions.

Table 3
Mean and standard deviation of projection and interpolation error with varied number of snapshots used for POD. The error is computed as L_2-norm error between PODI prediction and CFD solutions.

No of snapshots (Total: 40)	Projection errors		Interpolation errors	
	$\bar{\epsilon}$	ϵ_{rms}	$\bar{\epsilon}$	ϵ_{rms}
20	5.18e−05	1.53e−05	7.77e−01	3.32e−01
24	5.74e−05	2.06e−05	8.27e−01	2.88e−01
28	5.42e−05	2.03e−05	7.97e−01	3.50e−01
32	4.81e−05	2.48e−05	8.22e−01	3.38e−01

2009; Adams et al., 2014). To compute the approximating coefficients, two approaches are practically popular in the literature, namely the *point collocation* and *pseudo-spectral projection* approaches. In the point collocation (PC) method, the weighting coefficients can be found by minimizing the approximating errors in the least square minimization fashion. It belongs to the class of stochastic regression in which the sampled approximation is equated to the function evaluation at the sampled input; thus providing an over-determined system of equations for weighting coefficients. In contrast, the pseudo-spectral projection (PS) approach explores the orthogonality of the polynomial basis functions to compute the weights. The computation of coefficients thus requires only function evaluations at a set of quadrature nodes and their specified corresponding weights. There are different quadrature rules for this purpose. For more details on the two approaches, one can refer to the earlier review Xiu (2009). In this work, we used the open-source implementations of PCE available in Chaospy (Feinberg and Langtangen, 2015) and Dakota package (Adams et al., 2014) for sampling and uncertainty quantification.

4.5. *Effects of uncertain wind conditions on plume spreading*

Using the above surrogate forward model and PCE approach, with the input uncertainty in wind conditions, we can effectively quantify the spread of gas plumes. Firstly assuming that the wind speed and direction are independent, the maximum spread distance of the gas plume can be computed for each parameter separately. Fig. 17 shows the mean and variance of the gas cloud spread with the changing of wind speed and direction taking into account the probability distribution of the other parameters (wind direction and speed respectively) using PCE with polynomial order 5. In this decoupled analysis, it can be seen that the maximum spread distance of the gas cloud increases linearly with the increase of wind speed; while the trend is nonlinear with changes in wind direction. The variance of spread distance does not change significantly with changes in wind speed given the uncertain input of wind direction. However, depending on the wind direction, the effects of uncertain wind speed can have a significant impact on the variation of spread distance. The largest variance is observed for southerly wind, which is consistent with the earlier analysis. It is also noted that both PC and PS approaches provide very similar results for the output uncertainty.

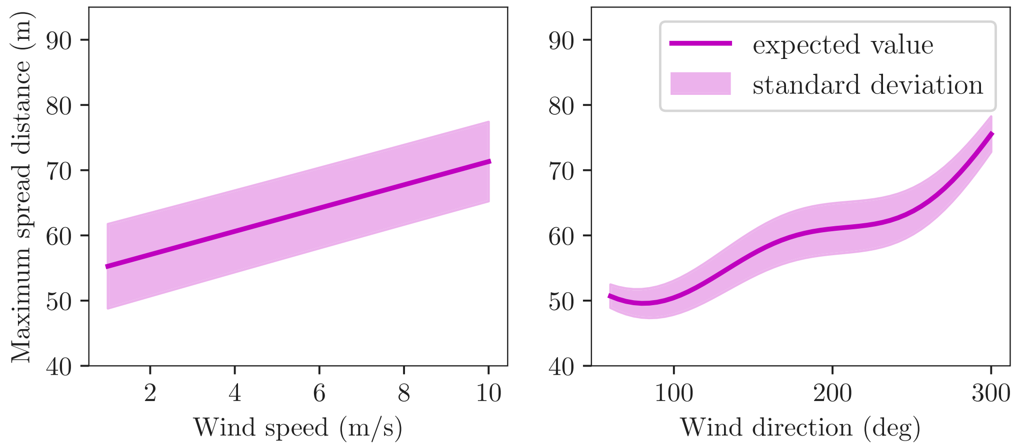

(a) Point collocation

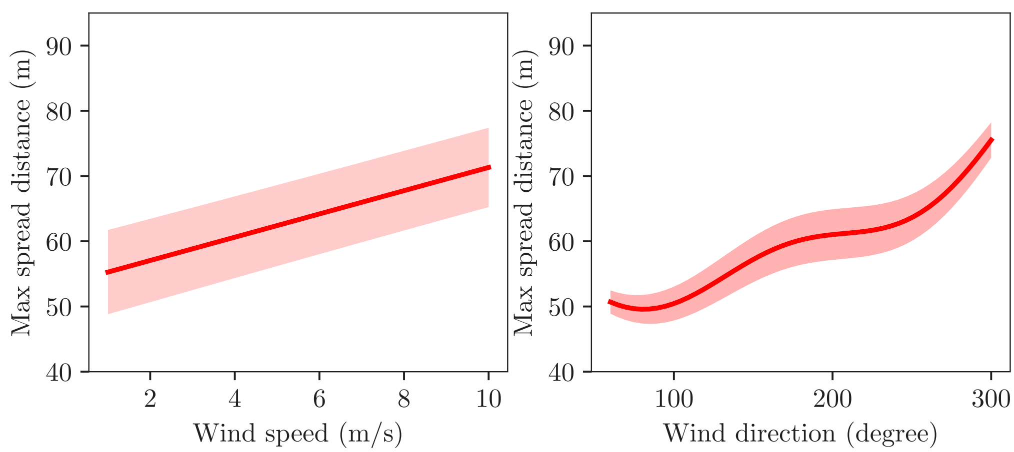

(b) Pseudospectral projection

Fig. 17. Maximum spread distance with wind speed and direction in decoupled (frozen) analysis.

It is however unlikely that wind speed and direction are independent. We next performed uncertainty quantification of gas plume spread in a joint probability distribution of wind speed and direction, taking into account their coupled effects. Fig. 18(a) shows the mean and variance of the spread of gas cloud with uncertain input of wind conditions with changing of approximating polynomial order using a PS PCE approach. For a polynomial order of larger than 3, it can be seen that the mean of the maximum spread converges to about 60.5 m with a variance of 6.8 m. The convergence of the analysis is further demonstrated in Fig. 18(b) where the error between PCE prediction for the mean and variance of maximum spread is compared with Monte-Carlo prediction. It is worth noting that the PC approach demonstrated instability at higher polynomial order (> 6) where the error suddenly jumped to a much larger value. In contrast, the PS approach does not suffer from this behaviour and shows good convergence of the variance error.

The current uncertainty in the maximum spread distance of 60.7 ± 6.8m exceeds most of the current safety guidelines in the operations of gas facilities. The above prediction tends to impose a more stringent restriction for space planning without taking into account the localized distribution of gas plumes. Fig. 19 depicts the spatial distribution of the mean and variance of LFL residence time under uncertain input of coupled wind speed and direction. It is clearly seen that the mean cloud residence time is higher near the north side of the enclosure while it is much lower in the south and south-west side. Similarly, the variance of the LFL residence time showed higher values in the north and north-east side of the enclosure. The results demonstrate the effects of both enclosure and uncertainty in wind direction on the spread of the gas plume. For one of the dominant winds, namely southerly wind, it is understandable that the gas cloud is likely to spread more in the north side of the enclosure. While for the other dominant direction (northerly wind), the enclosure prevents the spread of the cloud from moving south of the enclosure. With these results, it is possible to better utilize the available space around the facility taking into account the effects of uncertainty in wind conditions in the risk assessment process.

5. Conclusions

This work presented a CFD approach for the simulation of LNG leakages typically required for the risk assessment process of LNG facilities. The CFD model is combined with a transient jet leak tool to simulate a more realistic scenario of leakage where the process is inherently dynamic and transient, especially with the presence of safety equipment (such as ESD). The approach was validated with the experimental data obtained from a horizontal jet leak of methane gas into the ambient showing its convergence and accuracy. The tool was applied for a case study of keyhole leak in a mock-up LNG bunkering station to evaluate the spread of hazardous gas clouds under different

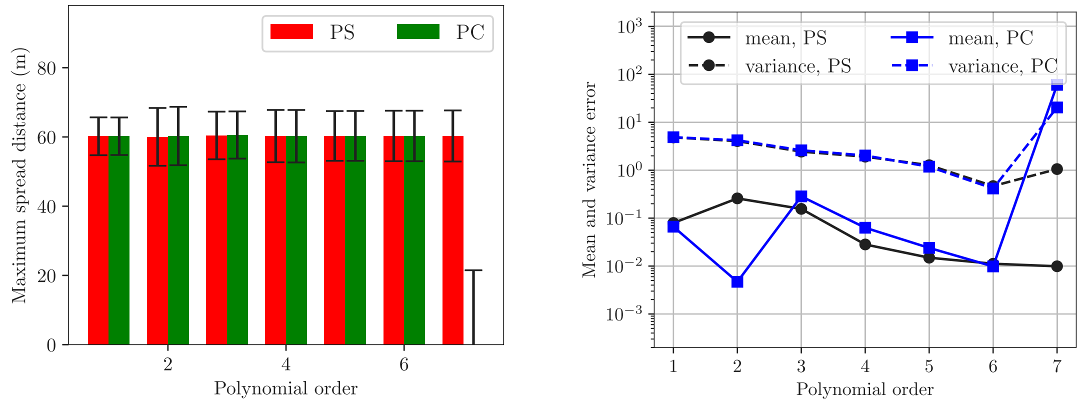

(a) mean and variance of spread distance (b) errors in mean and variance

Fig. 18. (a) Sensitivity of mean and variance of maximum spread distance with polynomial order for point collocation (PC) and pseudo-spectral projection PS PCE; and (b) their corresponding errors compared with Monte-Carlo simulations.

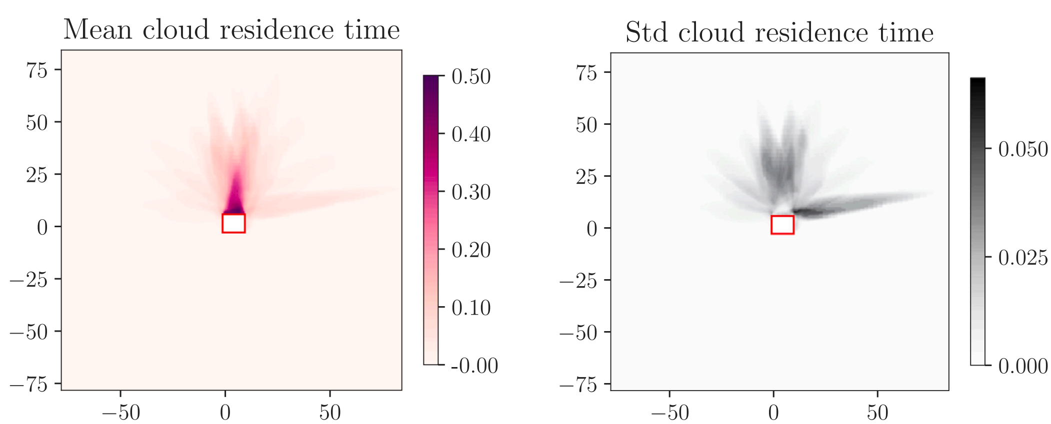

Fig. 19. Mean and standard deviation of LFL residence time (s) in the domain with uncertainty in both wind speed *and* direction.

wind conditions. Given the uncertainties in the wind conditions, the CFD results were used for uncertainty quantification of gas plume spread using the PCE approach. A ROM based on POD interpolation technique was developed for fast evaluation of gas cloud spreading for a given input wind condition. The uncertainty in the maximum spread of the gas plume was computed for independent input parameters of wind speed and direction; as well as for their joint probability distribution. Results from uncertainty quantification analyses showed the potential of the approach for quantitative risk analysis of LNG facilities given uncertain input parameters.

CRediT authorship contribution statement

Vinh-Tan Nguyen: Conceptualization, Methodology, Validation, Formal analysis, Writing – original draft, Writing – review & editing. **Venugopalan S.G. Raghavan:** Methodology, Validation, Formal analysis, Writing – original draft, Writing – review & editing. **Raymond Y.L. Quek:** Methodology, Validation, Formal analysis, Writing – original draft, Writing – review & editing. **Lim Boon How:** Formal analysis, Writing – review & editing. **Deguang Yan:** Formal analysis, Writing – review & editing.

Declaration of competing interest

The authors declare that they have no known competing financial interests or personal relationships that could have appeared to influence the work reported in this paper.

Acknowledgement

This research is partially supported by A*STAR under its Industry Alignment Fund - Industry Collaboration Projects Programme (Award I2101E0003). Any opinions, findings and conclusions or recommendations expressed in this material are those of the author(s) and do not reflect the views of the A*STAR. All authors have read and agreed to the published version of the manuscript.

References

Climate of Singapore, http://www.weather.gov.sg/climate-climate-of-singapore/, 2020-06-18.

Adams, B.M., Ebeida, M.S., Eldred, M.S., Jakeman, J.D., Swiler, L.P., Eddy, J.P., 2014. Dakota, A Multilevel Parallel Object-Oriented Framework for Design Optimization , Parameter Estimation , Uncertainty Quantification , and Sensitivity Analysis Version 6.7 Theory Manual. Sandia Technical Report SAND2014-4633, July, URL https://dakota.sandia.gov/sites/default/files/docs/6.7/Theory-6.7.0.pdf.

Animah, I., Shafiee, M., 2020. Application of risk analysis in the liquefied natural gas (LNG) sector: An overview. J. Loss Prev. Process Ind. 63 (August 2019), 103980. http://dx.doi.org/10.1016/j.jlp.2019.103980.

Anon, 2016. QRA Technical guidance. pp. 1–39, November, URL https://www.nea.gov.sg/docs/default-source/our-services/qra-technical-guidance_nov16.pdf.

Chinesta, F., Huerta, A., Rozza, G., Willcox, K., 2017. Model reduction methods. Encyclopedia Of Computational Mechanics Second Edition. pp. 1–36. http://dx.doi.org/10.1002/9781119176817.ecm2110.

Eberwein, R., Rogge, A., Behrendt, F., Knaust, C., 2020. Dispersion modeling of LNG-Vapor on land – a CFD-Model evaluation study. J. Loss Prev. Process Ind. 65, http://dx.doi.org/10.1016/j.jlp.2020.104116.

Feinberg, J., Langtangen, H.P., 2015. Chaospy: An open source tool for designing methods of uncertainty quantification. J. Comput. Sci. 11, 46–57. http://dx.doi.org/10.1016/j.jocs.2015.08.008.

Franquet, E., Perrier, V., Gibout, S., Bruel, P., 2015. Free underexpanded jets in a quiescent medium: A review. Prog. Aerosp. Sci. 77, 25–53. http://dx.doi.org/10.1016/j.paerosci.2015.06.006.

Giannissi, S.G., Venetsanos, A.G., Markatos, N., Bartzis, J.G., 2013. Numerical simulation of LNG dispersion under two-phase release conditions. J. Loss Prev. Process Ind. 26 (1), 245–254. http://dx.doi.org/10.1016/j.jlp.2012.11.010.

Helton, J.C., Johnson, J.D., Oberkampf, W.L., 2004. An exploration of alternative approaches to the representation of uncertainty in model predictions. Reliab. Eng. Syst. Saf. 85 (1–3), 39–71. http://dx.doi.org/10.1016/j.ress.2004.03.025.

Huser, A., Nilsen, P.J., Skåtun, H., 1997. Application of kϵ model to the stable ABL: Pollution in complex terrain. J. Wind Eng. Ind. Aerodyn. 67–68 (November), 425–436. http://dx.doi.org/10.1016/S0167-6105(97)00091-3.

Koopman, R.P., Ermak, D.L., 2007. Lessons learned from LNG safety research. J. Hazard. Mater. 140 (3), 412–428. http://dx.doi.org/10.1016/j.jhazmat.2006.10.042.

Luketa-Hanlin, A., Koopman, R.P., Ermak, D.L., 2007. On the application of computational fluid dynamics codes for liquefied natural gas dispersion. J. Hazard. Mater. 140 (3), 504–517. http://dx.doi.org/10.1016/j.jhazmat.2006.10.023.

Society for Gas as a Marine Fuel, 2018. Recommendation Of Controlled Zones During Lng Bunkering.

McInerney, E.H., Hart, R.J., Morrison, D.T., Kytomaa, H.K., 2014. New quantitative risk criteria for US LNG facilities. Process Saf. Prog. 33 (3), 237–246. http://dx.doi.org/10.1002/prs.11657, URL http://doi.wiley.com/10.1002/prs.11657.

Parente, A., Gorlé, C., van Beeck, J., Benocci, C., 2011. Improved k-ϵ model and wall function formulation for the RANS simulation of ABL flows. J. Wind Eng. Ind. Aerodyn. 99 (4), 267–278. http://dx.doi.org/10.1016/j.jweia.2010.12.017.

Park, S., Jeong, B., Yoon, J.Y., Paik, J.K., 2018. A study on factors affecting the safety zone in ship-to-ship LNG bunkering. Ships Offshore Struct. 13, 312–321. http://dx.doi.org/10.1080/17445302.2018.1461055, URL https://www.tandfonline.com/doi/abs/10.1080/17445302.2018.1461055.

Ruffin, E., Mouilleau, Y., Chaineaux, J., 1996. Large scale characterization of the concentration field of supercritical jets of hydrogen and methane. J. Loss Prev. Process Ind. 9 (4), 279–284. http://dx.doi.org/10.1016/0950-4230(96)00018-6.

Sun, B., Utikar, R.P., Pareek, V.K., Guo, K., 2013. Computational fluid dynamics analysis of liquefied natural gas dispersion for risk assessment strategies. J. Loss Prev. Process Ind. 26 (1), 117–128. http://dx.doi.org/10.1016/j.jlp.2012.10.002.

Thomson, H., Corbett, J.J., Winebrake, J.J., 2015. Natural gas as a marine fuel. Energy Policy 87, 153–167. http://dx.doi.org/10.1016/j.enpol.2015.08.027.

Wilcox, D.C., 2006. Turbulence Modeling For CFD. DCW Industries, p. 522.

Woodward, J.L., Pitblado, R.M., 2010. LNG Risk Based Safety: Modeling And Consequence Analysis. Wiley, http://dx.doi.org/10.1002/9780470590232.

Xiu, D., 2009. Fast numerical methods for stochastic computations: A review. Commun. Comput. Phys. 5 (2–4), 242–272.

Xu, J., Testa, D., Mukherjee, P.K., 2015. The use of LNG as a marine fuel: The international regulatory framework. Ocean Dev. Int. Law 46 (3), 225–240. http://dx.doi.org/10.1080/00908320.2015.1054744, URL https://www.tandfonline.com/doi/full/10.1080/00908320.2015.1054744.